Magnetic Model Calibration and Distortion Compensation for Electromagnetic Tracking in a Clinical Environment

Marco Cavaliere[1,2], Daragh Crowley[1,2], Herman Alexander Jaeger[1,2], Kilian O'Donoghue[2], and Pádraig Cantillon-Murphy[1,2]

[1]Department of Electrical and Electronic Engineering, University College Cork, T12K8AF Cork, Ireland
[2]Microelectronic Circuits Center Ireland (MCCI), Tyndall National Institute, T12R5CP Cork, Ireland

Electromagnetic tracking (EMT) of surgical tools is used for image-guided navigation in minimally invasive interventions. Calibration of the tracker position and orientation is a fundamental task to correct systematic errors. This article explores the effect of metallic distortion on the open hardware Anser EMT system and describes a newly developed approach for volume calibration of the magnetic field model. The technique is also applied to effectively map the field in the presence of magnetic shields that can be used to reduce electromagnetic distortions passively. Unlike calibration techniques commonly found in literature, which aim to correct the tracking position error, our method can reconstruct an analytical magnetic field model starting from a reduced amount of scattered data. This way, a faster convergence of the solver algorithm is obtained, and EMT position and orientation errors are inherently corrected. The new modeling technique was applied to generate a new, undistorted magnetic field model for Anser EMT, to demonstrate the effectiveness of passive shielding, and to compensate for the distortion introduced by a commercial fluoroscopy C-arm. Furthermore, the concept of a real-time distortion compensation technique is expressed based on the modeling method presented in this article. For all the experiments, sub-millimeter errors were obtained after calibration, which may meet the needs of most endoscopic and surgical navigation tasks.

Index Terms— **Electromagnetic modeling, electromagnetic tracking (EMT), magnetic shielding, minimally invasive medicine.**

NOMENCLATURE

EMT	Electromagnetic tracking.
ROI	Region of interest.
FG	Field generator.
EC	Emitter coil.
CU	Control unit.
RMSE	Root mean square error.
N-RMSE	Normalized RMSE.
MAE	Mean absolute error.
N-RMSE	Normalized MAE.
ME	Mean error.
PRC50	50th percentile (or median).
PRC95	95th percentile.
cdf	Cumulative distribution function.
DoF	Degrees of freedom.

I. INTRODUCTION

ELECTROMAGNETIC tracking (EMT) is the gold-standard technology used in minimally invasive surgery to localize instruments inside the human body without the requirement for line-of-sight, such as in flexible endoscopes, catheters, and robotic capsules [1], [2].

The main components of an EMT system are an FG, magnetic sensors used as tracking markers, and a CU to process the data. Usually, the ECs in the FG are designed to generate magnetic fields that can be well approximated by simple models, e.g., magnetic dipoles [3], [4], [5], current sheets [6], loops [7], or current filaments [8], [9]. Sensors used in clinical applications are miniature inductive pick-up coils [10], [11], and their position and orientation are calculated as an inverse problem from the field measurements, given the known magnetic field in the ROI.

Under standard conditions, systematic tracking errors can be due to the inability of the theoretical models to describe the real magnetic field. Moreover, the presence of conductive or ferromagnetic materials can modify the field shape, causing deviation from the ideal model. Either case can be considered a magnetic distortion because the magnetic model used for tracking is different from the real field measured by the sensor.

System calibration is a fundamental task aimed at compensating for systematic tracking errors due to imperfect modeling or caused by magnetic distortions in a given clinical environment [12]. Calibration can be obtained on two levels: by correcting the tracked position and orientation or by adjusting the field model to match the field measurements.

In the first case, the EMT error is evaluated within the ROI, and an error map is created from the distorted EMT pose to the compensated one. Reference positions can be physically defined by a calibration phantom or by a robotic system, or obtained using an accurate, undistorted tracking system, such as an optical tracking system. Several techniques have been proposed to build the distortion map, and the reader is directed to [13] for a complete review of EMT error mapping techniques.

Calibration approaches based on the correction of the tracking sensor position are suitable for low to mild distortion scenarios, while they cannot be used for highly distorted environments when the mismatch between the model and

Manuscript received 8 April 2022; revised 20 January 2023; accepted 1 May 2023. Date of publication 11 May 2023; date of current version 28 June 2023. Corresponding author: M. Cavaliere (e-mail: m.cavaliere.ucc@gmail.com).

Color versions of one or more figures in this article are available at https://doi.org/10.1109/TMAG.2023.3275297.

Digital Object Identifier 10.1109/TMAG.2023.3275297

the real magnetic field is such that the tracking algorithm may converge to local minima or not converge at all. For example, high static distortions could be caused by the presence of nearby electronics [14] or when a magnetic shield is employed [15], [16]. In these cases, a characterization of the field generated by the system is required [17], where a field map is generated based on FEA simulations or experimental measurements at reference positions in the workspace. Additional advantages of creating a field map rather than an error map are: 1) the field is only a function of the location and not of the sensor orientation; 2) a faster convergence of the tracking algorithm; and 3) both tracking position and orientation errors are automatically corrected. Methods of building a data-driven field model include interpolation of a lookup table [18], artificial neural networks [14], random forest [19], and convolutional neural networks [20].

The main drawback of volume characterization methods, either based on position error or field maps, is that data collection is time-consuming. Although volume characterization can be effectively used for factory calibration or for the initial system setup in a new environment, it is not suitable in dynamic scenarios where the position of the distorters may change frequently, and it is challenging and costly to integrate into clinical workflows.

One way to possibly overcome the limitations of characterization is to use a physics-based model of the field to reduce the number of DoF and, therefore, the amount of data to collect. In this case, it is not required for the data points to lie on precise grids, homogeneously distributed within the ROI or to use orthogonal three-axis sensors because the model calibration is achieved by using the real field measurements to fit parameters to a structured magnetic model. Moreover, the limited number of fitting parameters can help reduce random measurement errors. For example, in a system where magnetic dipoles represent the ECs, the free calibration parameters might be the position, orientation, and magnetic moment of the dipoles, like in a reverse tracking problem [21], [22]. However, this approach cannot always capture local variations of the tracking error, due to the limits of the simplified model, especially in proximity to the FG, or due to the presence of static distorters.

This article presents a modeling technique to fit a physics-based field model. The technique is flexible enough to adapt to different kinds of distortion scenarios. The technique is applied to perform factory calibration of the Anser EMT system [23] under standard conditions, to build a data-driven model of magnetic shields used for passive protection, and to compensate for the static distortion introduced by a fluoroscopy imaging system in a clinical environment. The reduced number of calibration parameters and reference sensors enables the intriguing potential for a real-time distortion compensation technique based on redundant measurements of external arrays of sensors [24]. Similar ideas have been expressed in many recent publications [25], [26], [27], but a practical working solution for field modeling has never been demonstrated. Real-time compensation techniques for dynamic distortions have been proposed, which make use of sensor arrays [28], [29], [30], simultaneous localization and tracking [31], artificial neural networks [32], [33], and fusion of inertial and magnetic sensors [34], [35], [36]. However, these methods are based on the correction of the tracked position. In contrast, the physical interpretation of the calibration model reduces the number of reference sensors required and enhances the extrapolation capabilities, both of which are essential factors for a real-time compensation technique where the real field inside the ROI is derived from field measurements collected at known positions around it.

In this article, we rst introduce the field modeling technique in Section II-A and the Anser EMT system used in the following experiments in Section II-B. In a laboratory environment, the technique was applied to interpolate field measurements for creating a magnetic model of the FG under undistorted conditions and in the presence of magnetic shields. In a clinical environment, after characterizing the tracking error introduced by a fluoroscopy imaging system, the shielding effect of the passive shields was demonstrated, and active compensation for the distortion was obtained using the new technique. Materials and methods used for the experiments are described in Section II, and the results are outlined in Section III. Finally, Section IV discusses the main findings, and Section V concludes the article.

II. Materials and Methods

A. Magnetic Model

The quasi-static magnetic field in a region free of current sources can be expressed as a gradient of a harmonic scalar potential [37], [38]. The potential is uniquely defined by the boundary conditions on a surface enclosing the volume. The boundary condition can be satisfied by the potential of a dipole density on the same surface [39], [40], [41]. The dipole density is equivalent to a distribution of surface currents [42]. However, when a finite number of field measurements are sampled from the magnetic field in the volume of interest, it is impossible to find a continuous dipole density. The surface must be discretized in a finite number of magnetic dipoles. If the position of the sources of the magnetic field and the distorters is known, it is convenient to place the magnetic dipoles at these locations. This choice accurately models the electric current distribution that generates the target magnetic flux density. The approximation works better if the currents are far from the ROI. In this way, the magnetic field can be expressed as the sum of the fields generated by a set of magnetic dipoles. The approximation can be seen as a series expansion, where the field of the dipoles constitutes basis functions that are linearly summed to fit the field samples.

The magnetic flux density, $\mathbf{B}$, generated by a magnetic dipole is expressed in the following equation:

$$\mathbf{B}(\mathbf{r}) = \frac{\mu_0}{4\pi}\left[\frac{3(\mathbf{m}\cdot\mathbf{u_r})\mathbf{u_r} - \mathbf{m}}{R^3}\right][T] \tag{1}$$

where $\mathbf{m} = X{\cdot}\mathbf{u_m}$ is the magnetic moment and $\mathbf{r} = R{\cdot}\mathbf{u_r}$ is the position vector that identifies the evaluation point relative to the dipole position. Magnitudes $X[A \cdot m^2]$ and $R[m]$ are scalars, and $\mathbf{u_m}$and $\mathbf{u_r}$ are unit vectors.

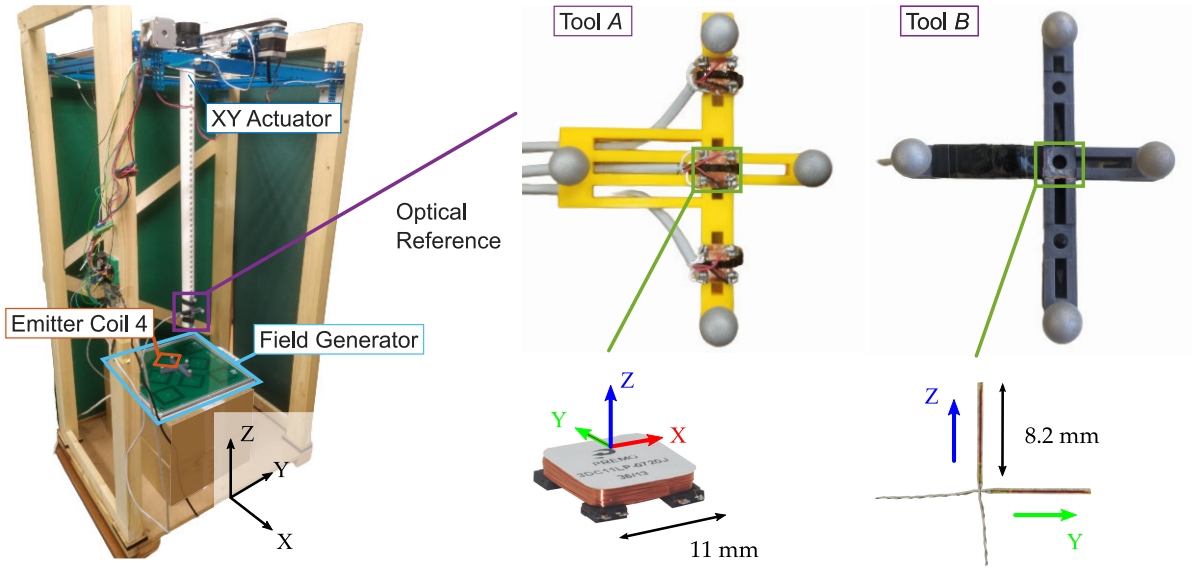

Fig. 1. Experimental setup in the laboratory environment. Tool A includes three triaxial sensor coils. Tool B is equipped with two uniaxial clinical-size sensors.

If the dipole magnitude X is isolated, (1) can be rewritten as follows:

$$\mathbf{B}(\mathbf{r}) = \frac{\mu_0}{4\pi}\left[\frac{3(\mathbf{u_m}\cdot\mathbf{u_r})\mathbf{u_r} - \mathbf{u_m}}{R^3}\right] X = f(\mathbf{r})X[T]. \quad (2)$$

Considering the magnetic sensor as a uniaxial inductive coil oriented along the unit vector $\mathbf{n}$, the field component is measured which is parallel to the sensor direction

$$V_s(\mathbf{r},\mathbf{n}) = k_s\mathbf{n}^{\mathrm{T}}\cdot\mathbf{B}(\mathbf{r})[V] \quad (3)$$

where k_s includes all the physical constants associated with the sensor gain, the magnetic field frequency, and the signal acquisition channel.

During calibration, a number P of sensor measurements are collected at different locations, $\mathbf{r}^{(i)}$, and with different sensor orientations, $\mathbf{n}^{(i)}$. The proposed method approximates the unknown magnetic field in the ROI as the field due to a set of N virtual magnetic dipoles placed at positions $\mathbf{r}^{(j)}$. According to this model, the ith sensor measurement is approximated as a sum of N contributions each calculated as per (2) and (3)

$$V_s^{(i)}\left(\mathbf{r}^{(i)},\mathbf{n}^{(i)}\right) = \mathbf{n}^{(i)\mathrm{T}}\cdot\sum_{j=1}^{N} f\left(\mathbf{r}^{(i)}-\mathbf{r}^{(j)}\right)X^{(j)}$$
$$= \sum_{j=1}^{N} f\left(\mathbf{n}^{(i)},\mathbf{r}^{(ij)}\right)X^{(j)}[V] \quad (4)$$

where $\mathbf{r}^{(ij)} = \mathbf{r}^{(i)} - \mathbf{r}^{(j)}$ is the relative position.

Equation (4) can be rewritten in matrix form by defining $\mathbf{M}$ as the P by N coupling matrix, whose entries M_{ij} are given by $f(\mathbf{n}^{(i)},\mathbf{r}^{(ij)})$ of (4), $\mathbf{X} = [\cdots X^{(j)}\cdots]^{\mathrm{T}}$, with $1 \le j \le N$, as the vector including the magnitudes of the dipoles, and $\mathbf{V_s} = [\cdots V_s^{(i)}\cdots]^{\mathrm{T}}$, with $1 \le i \le P$, as the vector including the field measurements. In this way, (4) becomes

$$\mathbf{V_s} = \mathbf{M}\cdot\mathbf{X} \quad (5)$$

which is solved for the dipole magnitudes that best fit the field measurements in a least-squares sense. When $P > N$, (5) is an overdetermined linear system that can be solved using typical methods for linear least-squares problems.

If there is no assumption on the orientations of the dipoles, the method can be extended by considering the three dipole components as independent dipoles. If the dipoles' positions are not fixed, they become part of the optimization process as independent variables in matrix $\mathbf{M}$. In this case, the problem is non-linear and can be solved using iterative methods. It is worth mentioning that the global problem where the magnetic flux density is calibrated in the ROI can be decomposed into smaller local problems where $\mathbf{X}$ is optimized for different sub-regions.

In this work, the position and orientation of the virtual dipole sources were defined in advance, and (5) was solved using the backslash operator in MATLAB

$$\mathbf{X} = \mathbf{M}\backslash\mathbf{V_s}. \quad (6)$$

B. Electromagnetic Tracking (EMT) System

Anser EMT is an open-source project aiming to be a platform for researching novel methods for EMT [23]. Anser EMT provides a cost-effective, open-hardware system used in this work to validate the proposed calibration method experimentally. The open-source system was used because the black-box nature of commercial tracking systems does not give access to the magnetic field measurements required to train the virtual dipole distribution used for static distortion compensation.

The Anser EMT CU includes the drive circuit to power the FG and the sense circuit to acquire magnetic field measurements and transmit the data to a computer. The FG is a two-layer planar printed-circuit board with an array of eight ECs, as depicted in Fig. 1. Each coil has a square shape and can be totally represented as a set of 100 straight tracks. The

magnetic field of every coil is independently modeled as the sum of the field due to straight current filaments [43], [44]. The coils are driven at different ac frequencies in a bandwidth that can be customized and was set from 6 to 7.2 kHz.

Two commercially available sensors were used in this work. A three-axis receiver coil (3DV11AOI-A-S0600J, Grupo Premo, Malaga, Spain) was chosen as a cost-effective solution to collect low-noise data quickly during the volume calibration. However, this sensor has a dimension of 1×1 cm^2, which is not compatible with the requirements for endoscopic applications. For this reason, a miniature coil (610158, Northern Digital Inc., Waterloo, Canada), with dimensions $\varnothing 0.45 \times 8.2$ mm length, was used when evaluating the EMT positional and angular accuracy.

In the case of both sensors, the inductive sensor is subject to a voltage proportional to the superposition of the eight ac magnetic fluxes linking the sensor coil. After demodulating the different frequency contributions, the fluxes can be used to train the magnetic field models during calibration or to find the sensor position and orientation for EMT. The sensor coils were connected to different acquisition channels of the CU and were previously calibrated to give consistent measurements.

The sensors were mounted on customized 3-D-printed dynamic reference frames [45]. One tool included three three-axis coils (Grupo Premo) spaced 3 cm, for a total of nine pick-up coils that could detect the eight magnetic fluxes from the ECs at the same time. A second tool was equipped with two miniature single-axis coils (NDI) with orthogonal orientations. In this article, we will refer to the two tools as tools A and B, respectively, as shown in Fig. 1.

The linear transformation between the reference frames' local coordinate systems and the sensors' locations was calculated by EMT in a non-distorted environment. The Polaris Vega optical system (Northern Digital Inc., Waterloo, Canada) provided ground-truth pose reference of the sensors and the FG. The system has a volumetric accuracy of 0.15 mm rms, declared by the manufacturer [46].

C. Experiments in the Laboratory Environment

The method presented in Section II-A was tested in a laboratory setting to demonstrate the capability to fit real field measurements and to predict new values.

The magnetic sensors were moved in two directions by two stepper motors controlled by Arduino hardware. A wooden structure kept the metallic motors at more than 1 m from the ROI to avoid magnetic field distortions. Tolerances of the motorized system did not add to the measurement uncertainty because the external optical system was used for position and orientation reference. The acquisition setup is shown in Fig. 1.

1) Novel Data-Driven Model for Anser EMT: As mentioned above, the magnetic model currently used by the Anser EMT system is based on the Biot–Savart law, under the assumption that each EC can be modeled by straight current filaments in the free space. In this experiment, a new analytical model was created for each EC. The model is based on a virtual distribution of magnetic dipoles whose magnitude was trained on real field measurements, as explained in Section II-A.

TABLE I
SHIELD PARAMETERS

Material	Conductivity (MS/m)	Relative permeability	Edge (mm)	Thickness (mm)
Aluminium	35	1	250	1
Mu-metal	1.8	>100000	250	1

Parameters of the two square planar shields used in this work.

Tools A and B were used for characterization and for tracking, respectively, to demonstrate that the magnetic model is generally independent of the sensor used as a tracking marker in the final application.

Tool A was used to collect a $31 \times 31 \times 3$ grid of points in a volume of $30 \times 30 \times 6$ cm^3 located 15 cm above the planar FG. A total of $P = 8649$ measurements per EC were collected and used for model training. The position of the virtual dipole sources was initialized in the proximity of the real position of the field generator. The number of dipoles was determined by optimizing the fitting performance at a selection of validation points randomly selected from the training set and not used for training. This way, the real magnetic field could be adequately modeled while avoiding overfitting. The optimal number resulted in $N = 12 \times 12 = 144$ dipoles. The fit was calculated as per (6).

A 2-D grid of 26×26 points was collected on a mid-plane of 25×25 cm^2, using Tool B with the two clinical-size sensors horizontally and vertically oriented relative to the FG along the Y and Z axes defined in Fig. 1, respectively. These measurements were used to test the EMT accuracy of the novel data-driven model compared to the previous analytical model.

The position error at each point was expressed as the Euclidean distance between the tracked position and the optical reference. The orientation error was expressed as the absolute angle between the tracked and real direction vectors.

Average position and orientation errors were expressed as the root-mean-square error (RMSE) and the ME over the total number of observations, P

$$\text{RMSE} = \sqrt{\frac{1}{P}\sum e^2}; \quad \text{ME} = \frac{1}{P}\sum e \tag{7}$$

where e is the position (or orientation) error at one test point.

Additional statistical measures were calculated to give an insight into the global error in the tested region, namely the median or PRC50 and the PRC95.

2) Modeling Highly Distorted Magnetic Fields: Magnetic shielding is commonly used to reduce the effect of metallic objects under the FG [47], [48]. The presence of a magnetic shield produces a distortion of the magnetic field, which must be accurately modeled prior to sensor tracking. Low-frequency ac magnetic fields, such as those used in the Anser EMT system, can be shielded by conductive or high-permeability materials or a combination of both [16]. The effects of aluminum and Mu-metal planar shields were studied. The parameters of the two plates are detailed in Table I.

As will be seen in Section III-A, the eddy currents appearing in the shields introduced a quadrature component to the ac magnetic field. The sum of out-of-phase vectors resulted in

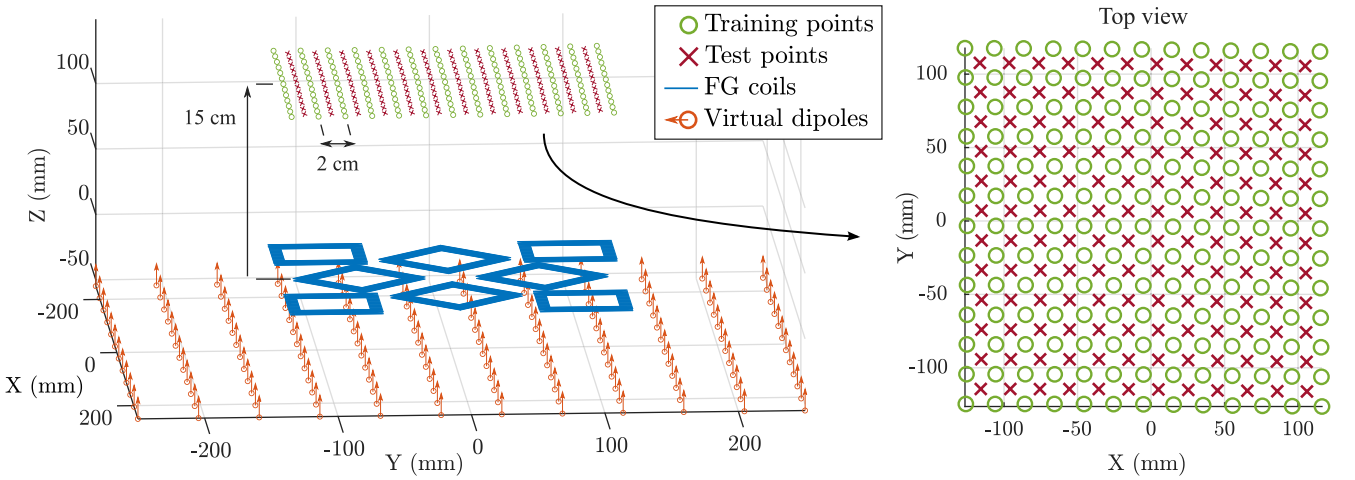

Fig. 2. Fit of the highly distorted magnetic field in the presence of metallic shields under the FG. The model was represented by an array of 12 × 12 magnetic dipole virtual sources, the magnitude of which was optimized to match the training point's magnetic measurements. Interpolation results were evaluated on the test points.

magnetic fields that rotated in ellipses at every point within the ROI. In this case, the three-axis coils of Tool A showed nonlinear behavior. It is believed that this has to be ascribed to the effect of the rotating field vectors on the larger ferromagnetic cores, causing crosstalk between the orthogonal coils.

For this reason, Tool B was used in this experiment, and the two uniaxial sensors in orthogonal directions provided the information to model the 3-D magnetic field vector. The fitting and interpolation performance of the proposed calibration technique was evaluated in the distorted scenario of the aluminum and Mu-metal planar shields placed below the FG.

A grid of points was sampled at a height of 15 cm above the FG. The measured data was split into a set of training points, used to calculate the virtual dipole sources distribution, and a set of test points for independent validation, as shown in Fig. 2.

The following metrics were used to evaluate the fitting performance on the training points and the interpolation effectiveness on the test points for the magnetic fields modeled. The MAE and the root-mean-square error (RMSE) were calculated by averaging the values from the two sensors and the eight ECs. The N-MAE and the N-RMSE were obtained by normalizing for the difference between the maximum and the minimum field values

$$\text{N-MAE} = \frac{1}{8P}\sum \text{abs}e/(\max e - \min e)$$
$$\text{N-RMSE} = \sqrt{\frac{1}{8P}\sum e^2}/(\max e - \min e) \quad (8)$$

where P is the total number of observations and e is the magnetic field difference at one test point.

As for the other tracking tests presented in this work, the error on the test points was also expressed in terms of positional and angular accuracy.

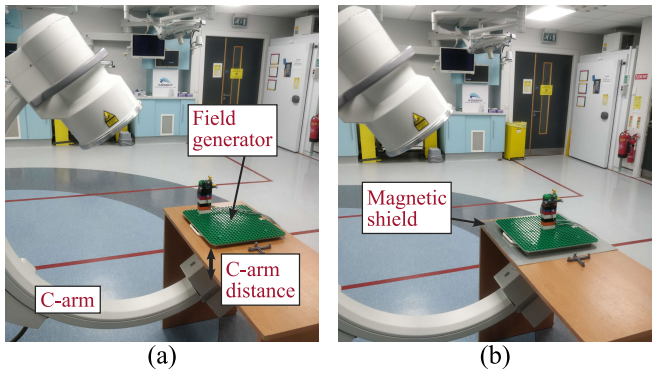

Fig. 3. (a) C-arm effect was evaluated at different distances from the FG, from an undistorted scenario to a minimum distance of 2 cm (maximum distortion). (b) Planar magnetic shield was placed below the FG as a possible solution against static and dynamic distorters.

D. Experiments in the Clinical Environment

The Anser EMT system was tested to demonstrate its performance when surrounded by metallic instruments commonly found in a clinical environment.

For these experiments, Tools A and B presented in Section II-B were mounted on Duplo blocks (The Lego Company, Billund, Denmark) and moved on a planar Duplo plate placed on the FG. The blocks served to keep the sensors stable at test points while taking the magnetic measurements and for moving the tools repeatedly and consistently. Even if positions on the Duplo grid have a defined spacing, the Polaris Vega optical system was used for ground-truth pose reference because it provided higher accuracy.

1) Distortion Introduced by the C-Arm: A mobile X-ray machine, also called C-arm in this article, is composed of metallic materials, both conductive and ferromagnetic, and can cause magnetic tracking errors which depend on the position of the machine.

The C-arm (GE OEC Fluorostar, General Electric Company, Boston, MA, USA) was moved at different distances from the tracking volume, from an undistorted scenario to a maximum distortion at 2 cm below the FG, as shown in Fig. 3(a).

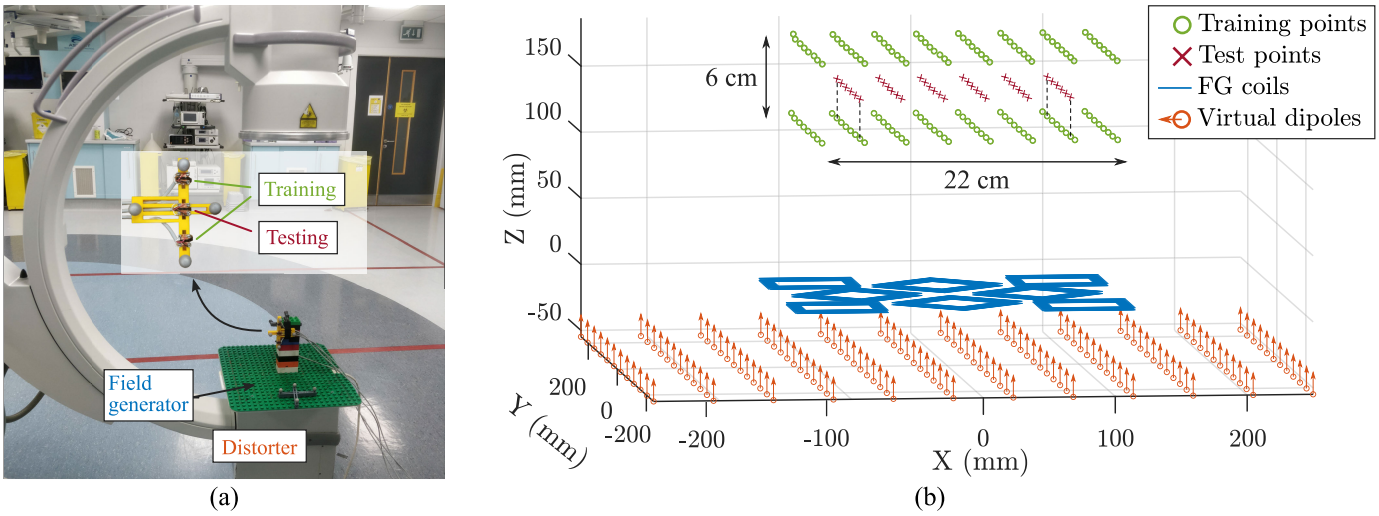

Fig. 4. Online distortion compensation technique. (a) FG was placed on top of the X-ray collimator, which introduced large metallic distortion. Tool A was used to measure the magnetic field on three parallel grids. (b) Top and bottom planes represent external sensors and were used to generate the field model which was then employed to find the position of the points in the midplane, for the EMT accuracy test with distortion compensation.

For every C-arm configuration, EMT tests were performed on a planar grid of 64 test points 15 cm above the FG. Tool B was used for the tracking test, with the two NDI miniature sensors oriented along the Y and Z axes, respectively. The uncompensated analytical field model based on the Biot–Savart law was used to infer the sensor position from the magnetic measurements. No shielding or compensation technique was applied.

2) Shielding Performance Against the C-Arm: The effectiveness of the aluminum and Mu-metal plates in shielding the ROI from the magnetic influence of the X-ray machine was tested.

The same experiment detailed in Section II-D1 was repeated, this time adding a shielding plate below the FG.

For each shield, a data-driven model was trained using the technique proposed in this article, while the C-arm was removed and did not introduce magnetic distortion. Then, the C-arm was moved 2 cm below the FG, as shown in Fig. 3(b), and the tracking test was carried out using the novel compensated data-driven magnetic field model.

3) Toward a Real-Time Distortion Compensation: The calibration method presented in this article was employed for the proof-of-concept of an online, i.e., during an EMT procedure, distortion compensation technique.

Tool A was used to sample three planes at 12, 15, and 18 cm above the FG, while the FG was placed directly above the C-arm, as shown in Fig. 4.

A data-driven magnetic model was trained on the data points of the top and bottom planes, and it was then used to perform a tracking test on the mid-plane test points.

In the envisioned application, redundant sensors will be placed around the tracking region, for example, integrated into external medical patches or embedded in the FG. Such reference sensors can calibrate the magnetic model in real-time, compensating for the effect of dynamic field distorters that affect the tracking of the internal sensors.

TABLE II
NEW ANALYTICAL MODEL

Model	Biot-Savart		Data-driven	
Orientation	**Y**	**Z**	**Y**	**Z**
RMSE (mm/deg)	0.93/0.61	1.03/0.80	0.28/0.23	0.23/0.21
ME (mm/deg)	0.76/0.45	0.93/0.71	0.20/0.20	0.20/0.17
PRC50 (mm/deg)	0.55/0.31	0.91/0.67	0.13/0.17	0.18/0.15
PRC95 (mm/deg)	2.04/1.43	1.69/1.32	0.62/0.45	0.39/0.42

Tracking test results using the new analytical data-driven model, compared to the current Anser EMT model based on Biot-Savart law. The position error of this test is also visualized in Fig. 5.

III. RESULTS

A. Experiments in the Laboratory Environment

1) Novel Data-Driven Model for Anser EMT: The tracking test showed an accuracy improvement with the new data-driven model, with respect to the previous analytical model based on the approximation of the ECs as sets of straight filaments.

Position and orientation error metrics are summarized in Table II, while Fig. 5 shows the empirical cdf of the position error, for the two models under test and for the two sensor orientations.

Using the novel magnetic field model, the position RMSE decreased from 0.93 to 0.28 mm (–69%) for the Y-oriented sensor and from 1.03 to 0.23 mm (–78%) for the Z-oriented sensor. The orientation RMSE decreased by –62% and –73%, respectively.

It can be noticed from Table II that the orientation error is, in general, highly correlated with the position error. This can be explained by the nature of the Anser EMT algorithm used to magnetically track uniaxial sensors, where a cost function is minimized to find the five DoF of the sensor simultaneously. For better readability, only the position error will be reported in the following tables presented in this article.

2) Modeling Highly Distorted Magnetic Fields: Fig. 6 shows the magnetic field of EC number 4 of the FG, which

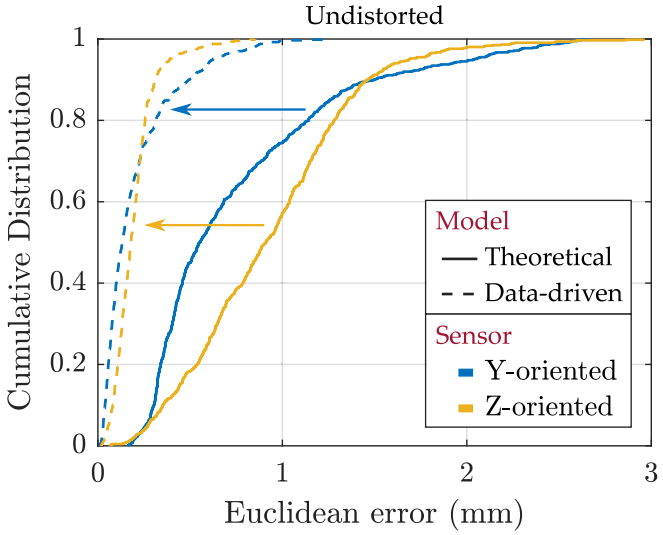

Fig. 5. EMT errors obtained with the new analytical data-driven model, compared to the current Anser EMT, in a distortion-free environment. Two commercial miniature sensors, *Y*- and *Z*-oriented (horizontal and vertical), were placed on a 25 × 25 cm^2 grid approximately 15 cm above the FG.

TABLE III
DISTORTED FIELD INTERPOLATION PERFORMANCE

Shield	Aluminium		Mu-metal	
Set	**Training**	**Test**	**Training**	**Test**
MAE (mA/m)	0.1377	0.2082	0.7827	1.4106
N-MAE (%)	0.0085	0.0131	0.0088	0.0160
RMSE (mA/m)	0.1885	0.2854	1.0817	1.8508
N-RMSE (%)	0.0116	0.0179	0.0122	0.0210
Orientation	**Y**	**Z**	**Y**	**Z**
RMSE (mm)	0.16	0.13	0.17	0.16
ME (mm)	0.11	0.11	0.12	0.14
PRC50 (mm)	0.07	0.09	0.09	0.12
PRC95 (mm)	0.32	0.27	0.36	0.29

Fitting results of the training data and interpolation performance at the test points, as defined in Fig. 2. For the test set, the magnetic field error is also translated to the correspondent tracking position error.

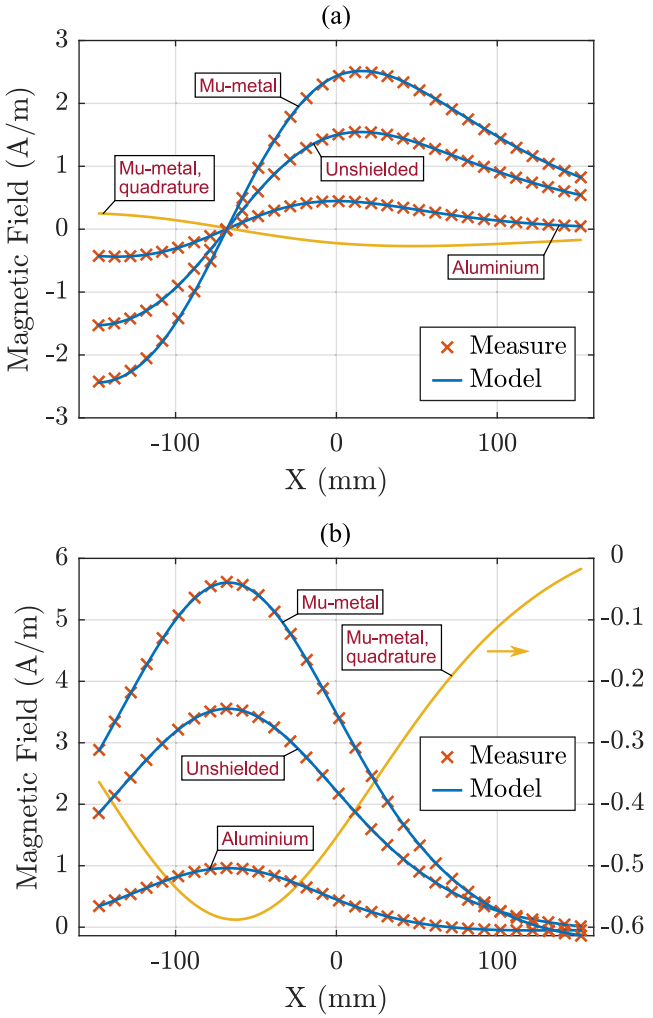

Fig. 6. Effect of shields on the magnetic field of the EC number 4, at $Y = 0$ mm and $Z = 150$ mm. (a) X component and (b) Z component of the field. The magnetic model presented in this article is used to fit the field measurements. The quadrature field component which appeared in the presence of the Mu-metal shield is plotted in yellow.

is the coil highlighted in Fig. 1, in the three cases of no shielding, and aluminum and Mu-metal plates placed below the FG. The X and Z components are plotted for a set of points at X from –15 to +15 cm, $Y = 0$ cm, and $Z = 15$ cm. The analytical model presented in Section II-A was used to fit the data points by training the virtual dipole distribution on the measured values, resulting in an accurate and smooth fit.

The effect of the aluminum and Mu-metal shields is apparent in decreasing and increasing the field magnitude, respectively. The eddy currents induced in the shields generated a quadrature ac field component, around one-tenth the magnitude of the main in-phase component. The quadrature component must be taken into consideration to avoid tracking errors. One solution is to synchronize to a specific signal phase, which must be consistent but does not necessarily have to be the direct phase. Fig. 6 shows the quadrature component for the Mu-metal shield case only because it is large enough to be appreciated.

Table III reports the fitting results of the training and test sets for the two shield materials. For the test points, the error is also expressed in terms of position accuracy, for the Y and Z sensor orientations.

B. Experiments in the Clinical Environment

1) Distortion Introduced by the C-Arm: The results of all the tracking tests with the C-arm at different distances are reported in Fig. 7, which shows the empirical cdf of the position error, for the Y and Z sensor orientations. As expected, the distorter effect increases when the C-arm is placed closer to the FG.

Distortion visualization was obtained using lattices of the tracked position [49], [50]. Fig. 8 shows the error map for the distortion introduced by the fluoroscopy C-arm placed 2 cm below the FG [Fig. 3(a)]. The ground truth and the tracked position of the test points are combined to form two meshes representing the undistorted (red) and distorted (black) volumes, respectively. The grids show the error evident in the X and Y directions. The color map is based on the total position error, calculated as the Euclidean distance.

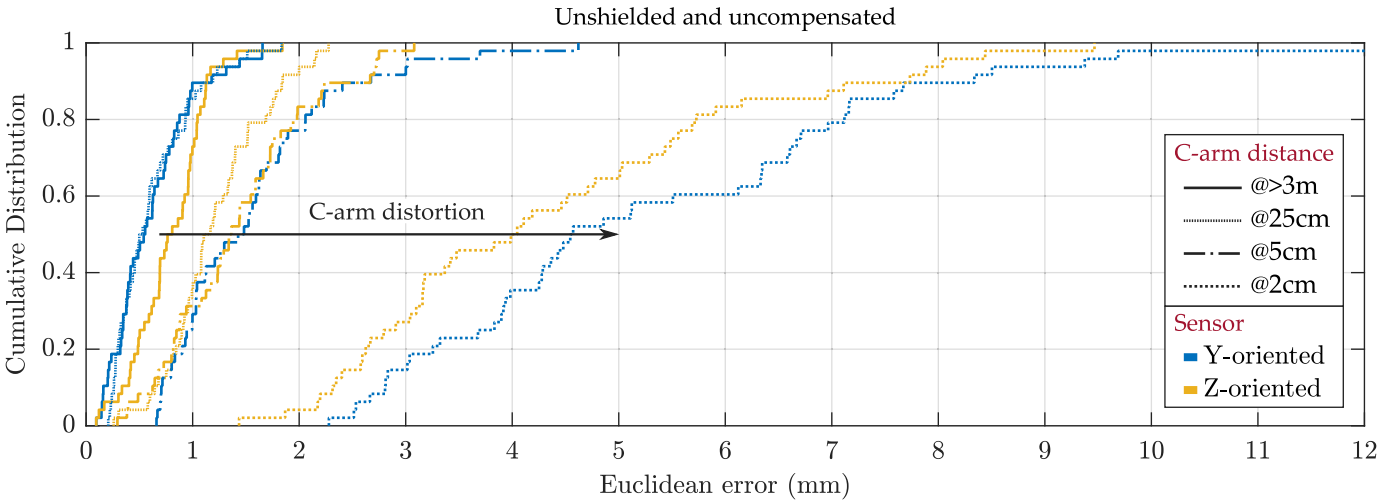

Fig. 7. Unshielded and uncompensated EMT error when the C-arm was moved closer to the FG, from a far position where it did not cause magnetic distortion to 2 cm (maximum distortion). The error distribution in the last case, when the fluoroscopy C-arm was placed at 2 cm, is visualized in Fig. 8. using meshes of the tracked and reference position, and must be compared to the error distribution obtained with magnetic shielding, shown in Fig. 9. The corresponding error metrics are reported in Table IV.

TABLE IV
PERFORMANCE IN SHIELDING THE C-ARM DISTORTION

Shield	Unshielded		Aluminium		Mu-metal	
Orientation	**Y**	**Z**	**Y**	**Z**	**Y**	**Z**
RMSE (mm)	5.72	4.74	0.31	0.46	0.23	0.51
ME (mm)	5.28	4.37	0.23	0.40	0.19	0.43
PRC50 (mm)	4.56	4.02	0.16	0.36	0.16	0.33
PRC95 (mm)	9.39	7.82	0.63	0.89	0.38	0.97

Tracking test results with the C-arm at 2 cm to show the effect of the shields. The position error of the unshielded case is visualized in Fig. 8, and the CDF of the three cases can be found in Fig. 7 (@2cm) and Fig. 9.

2) Shielding Performance Against the C-Arm: Fig. 9 shows the empirical cdf of the position error when the magnetic shields were used to block the C-arm distortion [Fig. 3(b)]. The error metrics are reported in Table IV, together with the tracking error obtained in the correspondent unshielded case.

Both shielding materials demonstrated effectiveness. A positional RMSE of 0.31/0.23 mm (aluminum/Mu-metal) was obtained for the Y-oriented sensor and an accuracy of 0.46/0.51 mm (aluminum/Mu-metal) for the Z-oriented sensor. These values must be compared with the RMSE of 5.72 and 4.74 mm obtained with Y- and Z-oriented sensors in the unshielded case.

3) Toward a Real-Time Distortion Compensation: Fig. 10 shows the empirical cdf of the tracking errors obtained when the FG was placed on top of the X-ray collimator, for the uncompensated case and after applying the distortion compensation technique.

It was observed that the unknown position and orientation errors were highly correlated with the errors of the points of the bottom plane, the real position of which is assumed to be part of the known training set. When correcting the unknown error of the midplane using the EMT information from the bottom plane, the tracking accuracy improved, as shown in Fig. 10(b).

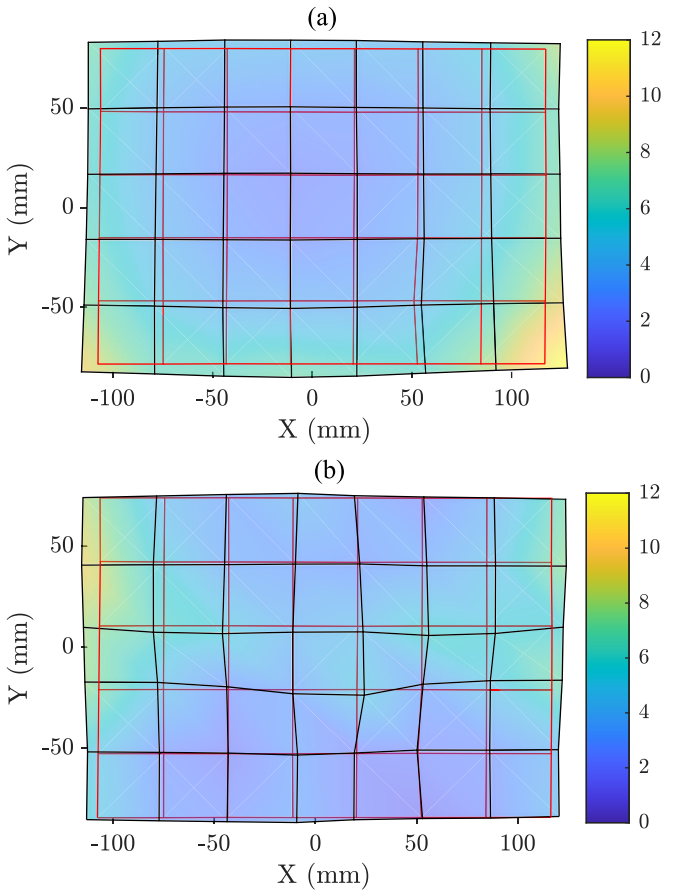

Fig. 8. Effect of the C-arm on the position tracking error when it was placed directly below (2 cm) the planar FG, without magnetic shielding or distortion compensation, when the magnetic sensor was (a) Y-oriented (horizontal) or (b) Z-oriented (vertical). The red grid is formed by joining the test-points and the black grid represents the tracked points. The color map (mm) also accounts for the error in the Z direction, which is not appreciable from the 2-D grids.

Position error results are reported in Table V, for the three cases compared.

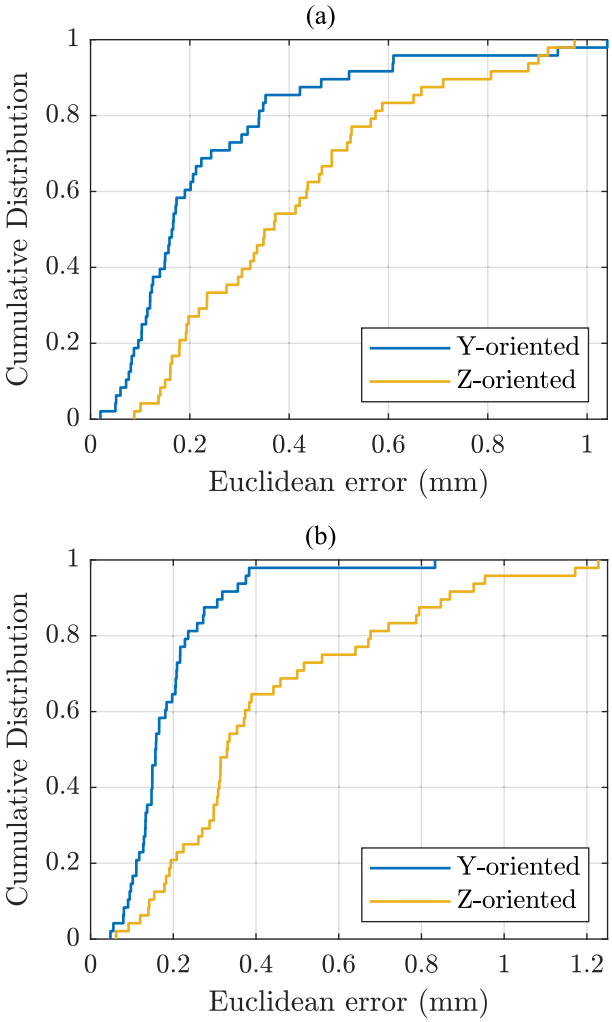

Fig. 9. Tracking errors when the fluoroscopy system was at minimum distance, 2 cm below the FG, using (a) aluminum plate and (b) Mu-metal plate to shield the distortion. The field model used to find the sensor position was trained on data collected in an undistorted environment where the fluoroscopy C-arm was removed.

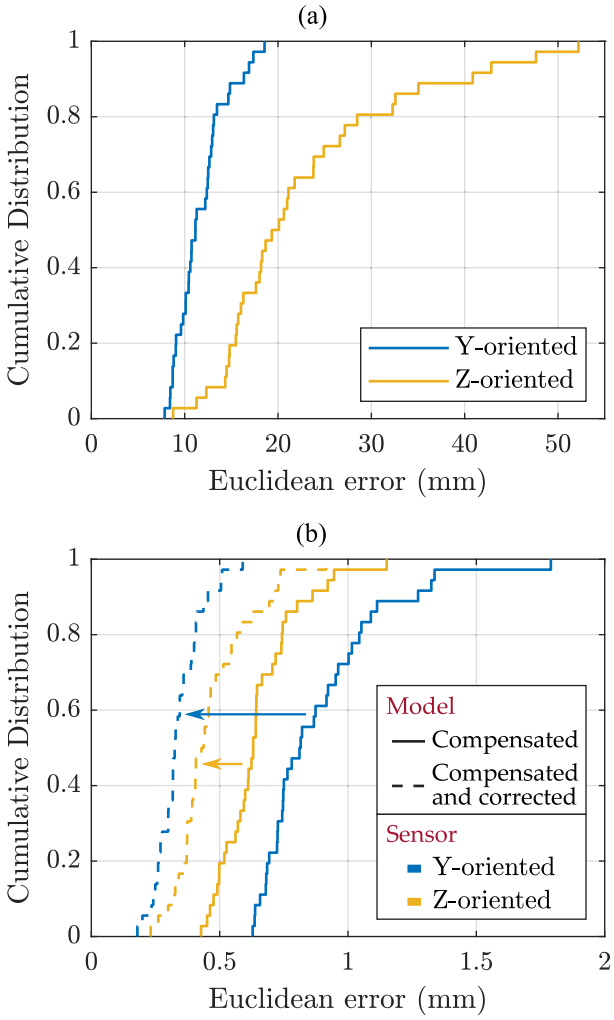

Fig. 10. Tracking errors when the FG was placed directly on top of the X-ray collimator. (a) High EMT errors are due to the presence of the fluoroscopy C-arm. (b) Errors obtained with the calibrated magnetic field model. The dashed lines show the further improvement obtained with the position correction based on the EMT solution of the points in the bottom plane.

TABLE V
REAL-TIME DISTORTION COMPENSATION

	Uncompensated		Distortion compensation		Compensated and corrected	
Orientation	**Y**	**Z**	**Y**	**Z**	**Y**	**Z**
RMSE (mm)	12.01	25.03	0.92	0.67	0.35	0.49
ME (mm)	11.71	22.87	0.89	0.65	0.34	0.47
PRC50 (mm)	11.15	19.71	0.81	0.63	0.33	0.43
PRC95 (mm)	17.22	46.21	1.33	0.94	0.51	0.73

Tracking test results with the field generator placed on top of the X-ray collimator, to show the effect of the distortion compensation technique. The CDF of the three cases is visualized in Fig. 10.

IV. DISCUSSION

The results presented above are commented on in this section, highlighting the main findings and their implications.

A consistent finding in all accuracy results obtained is that the EMT errors are typically smaller when the sensor is oriented horizontally along the Y axis. This is believed to be a result of the FG's shape and the configuration of the ECs, rather than differences in the sensors or acquisition channels.

The new data-driven model for Anser EMT FG demonstrated a higher tracking accuracy within the region tested. However, before updating the existing model, the calibrated model must be expanded to cover a larger volume.

Both shielding materials under test demonstrated effectiveness against large field distorters placed under the shielded FG. As expected, the magnetic field in the region above the FG was increased when using the Mu-metal shield and reduced with the aluminum shield.

This is due to different shielding working principles. Mu-metal provides a path for magnetic field lines rather than blocking them. The material becomes magnetized along the field direction, adding to the effect of the FG. Aluminum provides a conductive path for eddy currents induced by ac-varying magnetic fields. These currents generate fields that oppose the original field, effectively reducing the overall magnetic field strength.

The field magnitude is typically regulated to match the safety levels allowed for human exposure to electromagnetic

fields [51]. In that case, the Mu-metal could be preferred to decrease the system power consumption.

However, other factors must be considered when choosing the optimal shielding material, depending on the final application. For example, the Mu-metal relative permeability is sensitive to temperature and mechanical stress and can be affected by magnetic saturation or demagnetization, causing a change in the field shape that must be recalibrated. This may not be a concern in applications where the system is calibrated often or if a real-time compensation technique like the one proposed in Section II-D3) is applied. Aluminum has the advantages of being lightweight, electrically and mechanically more stable over time, cost-effective, and more translucent to X-rays [52].

Other shielding solutions are also possible, including nonconductive high-permeability materials, the combination of materials on different layers, and different configurations for the shielding plate dimension and distance from the FG. However, they were not analyzed in this study.

The experiment of the unshielded FG placed on top of the X-ray collimator demonstrated the interpolation performance of the magnetic model proposed in this article, that, starting from the information collected on two planes spaced 6 cm, allowed EMT on the midplane with sub-millimeter errors.

This opens the possibility of a real-time distortion compensation technique based on the magnetic measurements of sensors placed at known locations. For example, redundant sensors could be inserted along the catheter or embedded into patches attached to the patient. An external undistorted tracking system, such as X-ray imaging or an optical camera, might be used for position reference. Once the magnetic model is calibrated, it is valid until the position of a metallic distorter is not changed.

When the location of the external distorter is unknown, an extension of the presented calibration method might optimize for the position of the virtual magnetic dipole sources other than the magnitude. Future work will further validate the real-time compensation technique, considering realistic distortion environments.

V. Conclusion

This work presented a technique to model a magnetic field in an ROI, starting from real measurements. The method is based on an underlying analytical model. As opposed to other interpolation techniques, it is not required for the data to be aligned on a regular grid or for the three field components to be sampled separately. If enough points are taken in the ROI, the training data can be scattered, and the sensor coil orientation can vary.

The technique was employed for different use cases. A new magnetic model was created for the Anser EMT planar FG and was compared to the existing model by showing the tracking accuracy obtained in the two cases.

The effect of aluminum and Mu-metal planar shields on the magnetic field was studied. Using the modeling technique presented in this article, it was demonstrated that two sensors in an orthogonal direction could provide enough information to model highly distorted 3-D magnetic fields.

The distortion introduced by a fluoroscopy system was analyzed for different distances to the FG in a clinical environment. It was proven that aluminum and Mu-metal plates could effectively shield the ROI in the presence of external distorters. Finally, it was shown that it is possible to correct the field model inside the ROI using data collected outside it, presenting the intriguing potential for a real-time distortion compensation technique based on redundant measurements of external arrays of sensors.

Acknowledgment

This work was supported in part by the Science Foundation Ireland under Grant 17/CDA/4771 and Grant TIDA17/4897 and in part by the European Union ERC-2020-COG under Award 101002225. Views and opinions expressed are however those of the author(s) only and do not necessarily reflect those of the European Union or the European Research Council. Neither the European Union nor the granting authority can be held responsible for them.

References

[1] A. Sorriento et al., "Optical and electromagnetic tracking systems for biomedical applications: A critical review on potentialities and limitations," *IEEE Rev. Biomed. Eng.*, vol. 13, pp. 212–232, 2020, doi: 10.1109/RBME.2019.2939091.

[2] X. Duan, "Magnetic tracking and positioning in endoscopy," in *Magnetic Materials and Technologies for Medical Applications*, A. M. Tishin, Ed. Sawston, U.K.: Woodhead Publishing, 2022, pp. 287–338, doi: 10.1016/B978-0-12-822532-5.00013-3.

[3] H. P. Kalmus, "A new guiding and tracking system," *IRE Trans. Aeronaut. Navigational Electron.*, vol. ANE-9, no. 1, pp. 7–10, Mar. 1962, doi: 10.1109/TANE3.1962.4201833.

[4] F. Raab, E. Blood, T. Steiner, and H. Jones, "Magnetic position and orientation tracking system," *IEEE Trans. Aerosp. Electron. Syst.*, vol. AES-15, no. 5, pp. 709–718, Sep. 1979, doi: 10.1109/TAES.1979.308860.

[5] E. Paperno, I. Sasada, and E. Leonovich, "A new method for magnetic position and orientation tracking," *IEEE Trans. Magn.*, vol. 37, no. 4, pp. 1938–1940, Jul. 2001, doi: 10.1109/20.951014.

[6] T. Schroeder, "An accurate magnetic field solution for medical electromagnetic tracking coils at close range," *J. Appl. Phys.*, vol. 117, no. 22, Jun. 2015, Art. no. 224504, doi: 10.1063/1.4922667.

[7] G. De Angelis, A. De Angelis, A. Moschitta, and P. Carbone, "Comparison of measurement models for 3D magnetic localization and tracking," *Sensors*, vol. 17, no. 11, p. 2527, Nov. 2017, doi: 10.3390/s17112527.

[8] P. T. Anderson, "A source of accurately calculable quasi-static magnetic fields," Ph.D. thesis, Dept./Program Elect. Comput. Eng., Univ. Vermont, Burlington, VT, USA, 2001.

[9] K. O'Donoghue et al., "Catheter position tracking system using planar magnetics and closed loop current control," *IEEE Trans. Magn.*, vol. 50, no. 7, pp. 1–9, Jul. 2014, doi: 10.1109/tmag.2014.2304271.

[10] M. Cavaliere. (2019). *New Sensor Design and Characterization for Electromagnetic Tracking in Image-Guided Interventions*. Magistrali biennali. Accessed: Feb. 18, 2022. [Online]. Available: http://tesi.cab.unipd.it/62970/

[11] H. A. Jaeger, K. O'Donoghue, and P. C. Murphy, "Induction sensor characterisation for electromagnetic tracking systems," in *Proc. IEEE Int. Instrum. Meas. Technol. Conf. (I2MTC)*, Ottawa, ON, Canada, May 2022, pp. 1–6.

[12] A. M. Franz, T. Haidegger, W. Birkfellner, K. Cleary, T. M. Peters, and L. Maier-Hein, "Electromagnetic tracking in medicine—A review of technology, validation, and applications," *IEEE Trans. Med. Imag.*, vol. 33, no. 8, pp. 1702–1725, Aug. 2014, doi: 10.1109/TMI.2014.2321777.

[13] V. V. Kindratenko, "A survey of electromagnetic position tracker calibration techniques," *Virtual Reality*, vol. 5, no. 3, pp. 169–182, Sep. 2000, doi: 10.1007/BF01409422.

[14] E. Whitmire, F. S. Parizi, and S. Patel, "Aura: Inside-out electromagnetic controller tracking," in *Proc. 17th Annu. Int. Conf. Mobile Syst., Appl., Services*, Seoul, South Korea, Jun. 2019, pp. 300–312, doi: 10.1145/3307334.3326090.

[15] P. T. Anderson, "Surgical navigation system with electrostatic shield," U.S. Patent 2008 0 287 771 A1, Nov. 20, 2008, Accessed: Sep. 11, 2020. [Online]. Available: https://patents.google.com/patent/US20080287771A1/en
[16] K. O'Donoghue and P. Cantillon-Murphy, "Planar magnetic shielding for use with electromagnetic tracking systems," *IEEE Trans. Magn.*, vol. 51, no. 2, pp. 1–12, Feb. 2015, doi: 10.1109/TMAG.2014.2352344.
[17] J. J. Abbott, E. Diller, and A. J. Petruska, "Magnetic methods in robotics," *Annu. Rev. Control, Robot., Auto. Syst.*, vol. 3, no. 1, pp. 57–90, May 2020, doi: 10.1146/annurev-control-081219-082713.
[18] H. Himberg, Y. Motai, and A. Bradley, "Interpolation volume calibration: A multisensor calibration technique for electromagnetic trackers," *IEEE Trans. Robot.*, vol. 28, no. 5, pp. 1120–1130, Oct. 2012, doi: 10.1109/TRO.2012.2198929.
[19] R. Yu et al., "Modeling electromagnetic navigation systems for medical applications using random forests and artificial neural networks," in *Proc. IEEE Int. Conf. Robot. Autom. (ICRA)*, May 2020, pp. 9251–9256, doi: 10.1109/ICRA40945.2020.9197212.
[20] S. L. Charreyron, Q. Boehler, B. Kim, C. Weibel, C. Chautems, and B. J. Nelson, "Modeling electromagnetic navigation systems," *IEEE Trans. Robot.*, vol. 37, no. 4, pp. 1009–1021, Aug. 2021, doi: 10.1109/TRO.2020.3047053.
[21] A. Plotkin, V. Kucher, Y. Horen, and E. Paperno, "A new calibration procedure for magnetic tracking systems," *IEEE Trans. Magn.*, vol. 44, no. 11, pp. 4525–4528, Nov. 2008, doi: 10.1109/TMAG.2008.2003056.
[22] T. Bien and G. Rose, "Algorithm for calibration of the electromagnetic tracking system," in *Proc. IEEE-EMBS Int. Conf. Biomed. Health Informat.*, Jan. 2012, pp. 85–88, doi: 10.1109/BHI.2012.6211512.
[23] H. A. Jaeger et al., "Anser EMT: The first open-source electromagnetic tracking platform for image-guided interventions," *Int. J. Comput. Assist. Radiol. Surgery*, vol. 12, no. 6, pp. 1059–1067, Jun. 2017, doi: 10.1007/s11548-017-1568-7.
[24] M. Cavaliere, H. A. Jaeger, K. O'Donoghue, and P. Cantillon-Murphy, "Planar body-mounted sensors for electromagnetic tracking," *Sensors*, vol. 21, no. 8, p. 2822, Apr. 2021, doi: 10.3390/s21082822.
[25] Z. Xiong, J. E. McGary, and J. Chen, "Self-correcting magnetic tracking in dynamic medical environments," *IEEE Trans. Magn.*, vol. 51, no. 2, pp. 1–9, Feb. 2015, doi: 10.1109/TMAG.2014.2345333.
[26] B. Ramachandran and A. K. Jain, "Distortion fingerprinting for EM tracking compensation, detection and error correction," U.S. Patent 9 522 045 B2, Dec. 20, 2016. [Online]. Available: https://patents.google.com/patent/US9522045B2/en
[27] M. R. Schneider and K. Fujioka, "Compensating for distortion in an electromagnetic tracking system," U.S. Patent 2019 0 242 952 A1, Aug. 8, 2019, Accessed: May 12, 2020. [Online]. Available: https://patents.google.com/patent/US20190242952A1/en
[28] E. Shen and J. Kruecker, "System for local error compensation in electromagnetic tracking systems," U.S. Patent EP2 005 208 B1, Aug. 16, 2017, Accessed: Sep. 20, 2021. [Online]. Available: https://patents.google.com/patent/EP2005208B1/en?q=System+for+local+error+compensation+electromagnetic+tracking+systems&oq=System+for+ local+error+compensation+in+electromagnetic+tracking+systems
[29] E. Shen, "System and method for dynamic metal distortion compensation for electromagnetic tracking systems," U.S. Patent 2011 0 270 083 A1, Nov. 3, 2011, Accessed: Sep. 20, 2021. [Online]. Available: https://patents.google.com/patent/US20110270083A1/en
[30] G. Shechter, "Electromagnetic tracking method and apparatus for compensation of metal artifacts using modular arrays of reference sensors," U.S. Patent 7 902 816 B2, Mar. 8, 2011, Accessed: Sep. 20, 2021. [Online]. Available: https://patents.google.com/patent/US7902816B2/en
[31] H. Sadjadi, K. Hashtrudi-Zaad, and G. Fichtinger, "Simultaneous electromagnetic tracking and calibration for dynamic field distortion compensation," *IEEE Trans. Biomed. Eng.*, vol. 63, no. 8, pp. 1771–1781, Aug. 2016, doi: 10.1109/TBME.2015.2502138.
[32] H. Krumb et al., "Leveraging spatial uncertainty for online error compensation in EMT," *Int. J. Comput. Assist. Radiol. Surgery*, vol. 15, no. 6, pp. 1043–1051, Jun. 2020, doi: 10.1007/s11548-020-02189-w.
[33] H. Krumb, D. Das, R. Chadda, and A. Mukhopadhyay, "Cycle-GAN for interpretable online EMT compensation," *Int. J. Comput. Assist. Radiol. Surgery*, vol. 16, no. 5, pp. 757–765, May 2021, doi: 10.1007/s11548-021-02324-1.
[34] H. Ren, D. Rank, M. Merdes, J. Stallkamp, and P. Kazanzides, "Multisensor data fusion in an integrated tracking system for endoscopic surgery," *IEEE Trans. Inf. Technol. Biomed.*, vol. 16, no. 1, pp. 106–111, Jan. 2012, doi: 10.1109/TITB.2011.2164088.
[35] Y. Zhang, K. Wang, J. Jiang, and Q. Tan, "Research on intraoperative organ motion tracking method based on fusion of inertial and electromagnetic navigation," *IEEE Access*, vol. 9, pp. 49069–49081, 2021, doi: 10.1109/ACCESS.2021.3068741.
[36] D. K. O'Donoghue, D. H. A. Jaeger, and D. P. C. Murphy, "Sensor fusion hardware platform for robust electromagnetic navigation," presented at the IEEE I2MTC 2022, Ottawa, Canada, May 2022.
[37] J. D. Jackson, *Classical Electrodynamics*, 3rd ed. New York, NY, USA: Wiley, 1999, pp. 174–236.
[38] J. Vanderlinde, *Classical Electromagnetic Theory*, 2nd ed. Dordrecht, The Netherlands: Kluwer Academic Publishers, 2004, pp. 26–28.
[39] J.-C. Nedelec, *Acoustic and Electromagnetic Equations: Integral Representations for Harmonic Problems*. New York, NY, USA: Springer, 2011, pp. 110–149.
[40] W. Hackbusch, *Integral Equations: Theory and Numerical Treatment*, 1st ed. Basel, Switzerland: Birkhäuser, 2012, pp. 253–265.
[41] *Double-layer potential—Encyclopedia of mathematics*. Accessed: Dec. 10, 2021. [Online]. Available: https://encyclopediaofmath.org/index.php?title=Double-layer_potential
[42] A. J. Mäkinen, R. Zetter, J. Iivanainen, K. C. J. Zevenhoven, L. Parkkonen, and R. J. Ilmoniemi, "Magnetic-field modeling with surface currents. Part I. Physical and computational principles of bfield-tools," *J. Appl. Phys.*, vol. 128, no. 6, Aug. 2020, Art. no. 063906, doi: 10.1063/5.0016090.
[43] H. A. Haus and J. R. Melcher, *Electromagnetic Fields and Energy*, vol. 107. Englewood Cliffs, NJ, USA: Prentice-Hall, 1989.
[44] C. L. W. Sonntag, M. Sprée, E. A. Lomonova, J. L. Duarte, and A. J. A. Vandenput, "Accurate magnetic field intensity calculations for contactless energy transfer coils," in *Proc. 16th Int. Conf. Comput. Electromagn. Fields*, Achen, Germany, Jul. 2007, pp. 1–4.
[45] A. Brown, A. Uneri, T. D. Silva, A. Manbachi, and J. H. Siewerdsen, "Design and validation of an open-source library of dynamic reference frames for research and education in optical tracking," *J. Med. Imag.*, vol. 5, no. 2, Apr. 2018, Art. no. 021215, doi: 10.1117/1.JMI.5.2.021215.
[46] *Polaris Vega—NDI*. Accessed: Mar. 30, 2022. [Online]. Available: https://www.ndigital.com/products/polaris-vega/
[47] W. S. Ashe, "Magnetic field permeable barrier for magnetic position measurement system," U.S. Patent 6 246 231 B1, Jun. 12, 2001, Accessed: Mar. 31, 2021. [Online]. Available: https://patents.google.com/patent/US6246231B1/en
[48] W. Ashe, "Magnetic position and orientation measurement system with magnetic field permeable attenuator," U.S. Patent 6 784 660 B2, Aug. 31, 2004, Accessed: Mar. 31, 2021. [Online]. Available: https://patents.google.com/patent/US6784660B2/en
[49] G. Zachmann, "Distortion correction of magnetic fields for position tracking," in *Proc. Comput. Graph. Int.*, 1997, pp. 213–220.
[50] V. Harish, T. Ungi, A. Lasso, A. MacDonald, S. Nanji, and G. Fichtinger, "Intraoperative visualization and assessment of electromagnetic tracking error," in *Proc. SPIE*, vol. 9415, 2015, Art. no. 94152H, doi: 10.1117/12.2082330.
[51] *IEEE Standard for Safety Levels With Respect to Human Exposure to Electric, Magnetic, and Electromagnetic Fields, 0 Hz to 300 GHz*, IEEE Standard C95.1-2019, Revision of IEEE Standard C95.1-2005/Incorporates IEEE Standard C95.1-2019/Cor 1-2019, Oct. 2019, pp. 1–312, doi: 10.1109/IEEESTD.2019.8859679.
[52] K. O'Donoghue, H. A. Jaeger, and P. Cantillon-Murphy, "A radiolucent electromagnetic tracking system for use with intraoperative X-ray imaging," *Sensors*, vol. 21, no. 10, p. 3357, Jan. 2021, doi: 10.3390/s21103357.

Marco Cavaliere (Member, IEEE) received the Laurea Magistrale degree in electrical energy engineering from the University of Padua, Padua, Italy, in 2019. He is currently pursuing the Ph.D. degree in electrical and electronic engineering with University College Cork, Cork, Ireland, and the Tyndall National Institute, Cork.

His current research interests include electromagnetic tracking and navigation for image-guided interventions, magnetic field modeling, and object tracking algorithms.

Dr. Cavaliere served as the Chair of the IEEE Student Branch of Cork from 2020 to 2022.

Daragh Crowley (Member, IEEE) received the B.E. degree in electrical and electronic engineering from University College Cork (UCC), Cork, Ireland, in 2021, where he is currently pursuing the Ph.D. degree in electrical and electronic engineering with the Tyndall National Institute, Cork.

His current research interests include electromagnetic tracking and navigation systems for image-guided interventions.

Herman Alexander Jaeger received the B.E., M.Eng.Sc., and Ph.D. degrees in electrical and electronic engineering from University College Cork (UCC), Cork, Ireland, in 2014, 2015, and 2018, respectively.

He is currently a Post-Doctoral Researcher with UCC. His current research interests include electromagnetic tracking and navigation for image-guided interventions.

Kilian O'Donoghue received the B.E. and Ph.D. degrees in electrical and electronic engineering from University College Cork, Cork, Ireland, in 2011 and 2015, respectively.

His research interests include EM tracking systems, circuit design, magnetic field modeling, and minimally invasive surgeries.

Pádraig Cantillon-Murphy (Senior Member, IEEE) received the B.E. degree (Hons.) in electrical and electronic engineering from University College Cork, Cork, Ireland, in 2003, and the M.Sc. and Ph.D. degrees from the Department of Electrical Engineering and Computer Science, Massachusetts Institute of Technology (MIT), Cambridge, MA, USA, in 2005 and 2008, respectively.

From 2008 to 2010, he was a Post-Doctoral Research Fellow with concurrent appointments at Brigham and Women's Hospital, Harvard Medical School, Boston, MA, USA, and the Research Laboratory of Electronics, MIT. This work examined the role of magnetics in minimally invasive surgical procedures. He is a Professor of Biomedical Engineering at University College Cork, an Academic Member with the Tyndall National Institute, Cork, and University College Cork, and a Honorary Faculty at l'Institut de Chirurgie Guidée par l'Image, Strasbourg, France. He is the Principal Investigator at the Biomedical Design Laboratory, UCC, and the Tyndall National Institute, which explores novel device development in image-guided surgery and endoscopy. He has co-founded two startup companies. His current research interests include electromagnetic tracking and navigation in image-guided interventions, and surgical robotics. His teaching interests include electronic circuits, electromagnetics, and biomedical design.

Dr. Cantillon-Murphy was a former Marie Curie fellow from 2010 to 2014, a former MIT Whitaker fellow from 2007 to 2008, and an ERC awardee in 2020. He serves on the International Steering Committee of SMIT and as an Irish Committee Representative on Commission K (Electromagnetics in Biology and Medicine) of URSI.